Scanning low-temperature element-specific magnetic microscopy

A. Cady,[a] D. Haskel, J. C. Lang, and G. Srajer
Advanced Photon Source, Argonne National Laboratory, Argonne, Illinois 60439

P. Chupas, R. Osborn, and J. F. Mitchell
Materials Science Division, Argonne National Laboratory, Argonne, Illinois 60439

J. S. Ahn, N. Hur, S. Park, and S.-W. Cheong
Department of Physics & Astronomy, Rutgers University, Piscataway, New Jersey 08854

(Received 13 January 2005; accepted 3 April 2005; published online 18 May 2005)

We have developed a low-temperature element-specific magnetic microscopy instrument at beamline 4-ID-D of the Advanced Photon Source. The setup enables simultaneous chemical and magnetic characterization of materials with $\sim 1\ \mu m^2$ resolution at low temperature (>10 K) under a moderate applied field (<0.8 T). We demonstrate the potential of this apparatus by presenting results correlating chemical and magnetic local behavior in inhomogeneous layered manganites and multiferroic systems. © *2005 American Institute of Physics.* [DOI: 10.1063/1.1921510]

I. INTRODUCTION

Many problems of current interest in magnetic materials relate to phase separation, percolation transitions, and correlating chemical and magnetic domains. In all these cases, understanding microscopic magnetic domain structure and its correlation with chemical composition is extremely important. The colossal magnetoresistance (CMR) properties exhibited by doped manganese oxides like $(La,Sr)MnO_3$, for example, are thought to arise from a competition between magnetic and charge/orbital correlations.[1] In addition, there has been speculation that the metal-to-insulator transition is due to a percolation transition and is dependent on magnetic domain growth.[2] Understanding the mechanisms behind this domain growth and the role that chemical inhomogeneities play in these intrinsically inhomogeneous doped systems needs to be further elucidated. Similarly, composite mixtures of ferromagnetic half-metallic perovskites like $La_{3/8}Sr_{5/8}MnO_3$ (LSMO) with antiferromagnetic insulating $LuMnO_3$ (LMO) have also been shown to exhibit CMR-type behavior.[3] Models of CMR suggest that it is intimately related to both the morphology of the chemical grains and the alignment of magnetic domains within the ferromagnetic grains.

To understand the phase separation in magnetic materials, and how chemical inhomogeneities are related to the phase separation, requires microscopic imaging techniques that probe both the chemical and magnetic domain structures under applied magnetic fields and at low temperatures. We have developed a hard x-ray microprobe that can be used to address these questions in a unique way while providing complementary information to other existing probes of magnetic microstructure. Photoelectron emission microscopy (PEEM), for example, has a very high level of spatial resolution,[4,5] but many of the currently available instruments have limited temperature range and applied magnetic field capabilities. PEEM also has the further limitation that it does not probe bulk magnetic properties since the detected electrons come from the top ≈ 50 Å of the sample. This can be a particularly important issue in studies of doped manganites, where surface oxygen concentration could be different than in the bulk. Other techniques, such as magneto-optical Kerr effect microscopy[5] and magnetic force microscopy[6,7] do not provide element-specific magnetic information. The requirement to simultaneously image microscopic chemical and magnetic domain structure in bulk samples has motivated the advancement of hard x-ray (5–10 keV) microfocusing techniques at beamline 4-ID-D of the Advanced Photon Source. In this article, we describe development of a hard x-ray scanning low-temperature element-specific magnetic microscopy instrument designed to provide such information.

Using this instrument, one can directly correlate chemical and magnetic structure in novel materials, such as complex oxides. In Sec. II, we describe the experimental setup and its unique characteristics. Section III includes two sets of experimental results presented to illustrate the capability and utility of the technique. The first result was obtained from a bilayer manganite system in which chemical inhomogeneities play a role in the CMR behavior and affect the paramagnetic-to-ferromagnetic transition. The second study was performed on multiferroic composite mixtures of ferromagnetic half-metallic perovskite LSMO and the antiferromagnetic insulating LMO. The results, discussed in Sec. IV, demonstrate the advantage of simultaneously imaging chemical and magnetic domains in inhomogenous magnetic materials.

II. EXPERIMENTAL TECHNIQUE AND SETUP

The magnetic microscopy instrument has been developed at beamline 4-ID-D of the Advanced Photon Source[8] due to the high photon flux, brilliance, and circular polarization available on this line. To couple to the magnetization in

[a]Author to whom correspondence should be addressed; electronic mail: acady@aps.anl.gov

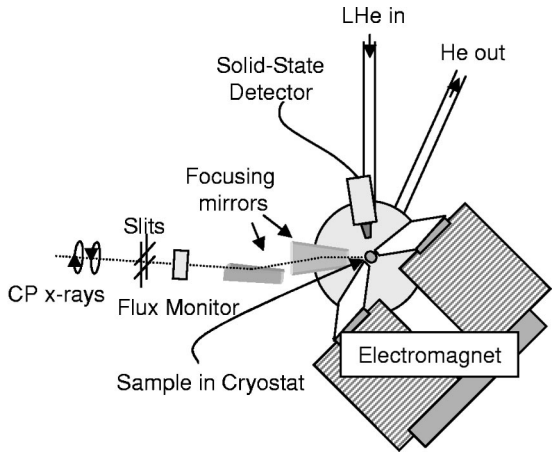

FIG. 1. The experimental setup at beamline 4-ID-D. The incident circularly polarized x rays pass through slits, defining the beam size to 250 $\times 250$ μm^2. The beam is then incident on mirrors that focus the beam vertically and horizontally to $\approx 4 \times 4$ μm^2. The focused beam is incident on the sample, which resides at the end of a cryostat cold finger, extending between the pole pieces of an electromagnet. Three energy-dispersive solid-state detectors were mounted above the sample to measure the fluorescence signal.

ferromagnetic samples, it is best to use a circularly polarized beam. At beamline 4-ID-D, a diamond (111) phase-retarding crystal is used in Bragg transmission geometry to convert incoming linearly polarized x rays from an APS planar undulator-A[9] to either left- or right-handed circularly polarized (LCP or RCP) x rays.[10] The reversal between LCP and RCP x-rays is rapidly achieved using a piezoelectric actuator to rotate the phase-retarding crystal slightly ($\sim$50 arcsec) above or below the exact Bragg condition.

A schematic of the main components of the magnetic microscopy setup is shown in Fig. 1. The incident, monochromatic, unfocused circularly polarized beam is defined using 250×250 μm^2 slits. The beam passes through a monitor detector and is subsequently focused by using a set of trapezoidal Kirkpatrick–Baez (KB) mirrors. Both the vertically and horizontally focusing mirrors are angled (3–9 mrad, depending on the energy of the x-ray photons) to satisfy total external reflection of the beam and bent meridionally to a correct curvature and ellipticity using submicron resolution actuators in order to focus the beam. The mirrors are based on a design developed by GeoSoilEnviroCARS (Sector 13) at the APS[11,12] and are made of single-crystal Si coated with Pd. The flux of the focused beam is approximately 10^{11} photons/s. This system provides a minimum focal spot size of $\sim 2 \times 3$ μm^2. Preserving this small beam size over many hours, however, requires refocusing the optics to compensate for small relaxations of the mirrors and bending mechanism. In the case of relaxed focusing requirements, a beam size of $\approx 4 \times 4$ μm^2 could be maintained over the course of several days needed to perform the types of measurements described in Sec. III.

The demagnification of each of the KB mirrors is equal to the distance from the x-ray source to the mirrors divided by the distance between the mirror and the focal point. For the vertical and horizontal KB mirror setup employed here, the optimal focal distance is 30 mm from the end of the second mirror. To take full advantage of the focusing capability of the mirrors we designed the experimental setup for the sample to be within 1–2 mm of the optimal focal distance. To fit a sample at low temperature in a moderate applied magnetic field at this small distance while maintaining optical access for the detectors above the sample required both a specially designed electromagnet and cryostat. A vibration-free helium-flow cryostat (10–300 K) was used to cool the sample. A vibration-free cooling method is essential for these measurements since imaging experiments require submicron stability of the sample position. The cryostat was originally designed for optical experiments (Janis Research Supertran System), but was modified with the addition of a cold-finger extension on the end of which the sample is mounted. This 108 mm extension allowed the sample to be placed between the magnet pole pieces, as shown in Fig. 1, and moved the cryostat body further away from the focusing optics. A beryllium vacuum shroud (19 mm in diameter) surrounds the sample. A silicon diode, mounted at the base of the cold finger served as a control sensor for the proportional integral differential (PID) temperature-control loop, and another silicon diode was mounted at the end of the cold finger near the sample position to record the sample temperature. The sample could be cooled to as low as 10 K with a stability on the order of 0.01 K. To cool to base temperature requires only 30–45 min. The entire cryostat assembly is mounted on *x*-, *y*-, and *z*-translation stages with 0.1 μm resolution, allowing the sample to be scanned through the incident x-ray beam.

To address a certain class of problems of interest in magnetism, one needs to apply a reasonably large magnetic field. Two geometrical constraints motivated the design of a specialized electromagnet. First, the gap in the pole pieces had to be large enough so that the 19-mm-diam cold finger of the cryostat could be moved about in a region of uniform field. Second, the center of the pole pieces had to be approximately 30 mm from the end of the horizontally focusing KB mirror. The resulting magnet has a gap of 21 mm between the pole pieces, allowing the sample position to be moved about ± 1 mm while remaining in a uniform magnetic field. The magnet conductor is water cooled, and 60 A of current can be used yielding magnetic flux densities of up to 0.8 T. The magnet was inclined so that it made a field at 45° to the horizontal direction. This moved the magnet windings away from the optics and increased the optical access.

A Vortex™ energy-dispersive silicon-drift diode detector with a 50 mm^2 active area manufactured by Radiant Technologies[13] was used to resolve the fluorescence lines with a resolution of 150 eV. The compact size of these detectors ($\sim 70 \times 70 \times 170$ mm^3) permitted the use of multiple detectors (up to three in these experiments) to monitor the fluorescence signal from the sample. The use of multiple detectors is especially important for the x-ray magnetic circular dichroism (XMCD) measurements, discussed in Sec. III, since they frequently involve the detection of very small difference signals in this energy regime (e.g., the Mn *K*-edge XMCD is only 0.1%). Accumulation of tens of millions of counts is required to achieve sufficient statistical precision in the difference signal. While these detectors are capable of count rates in excess of 500 kHz, they have to be limited to

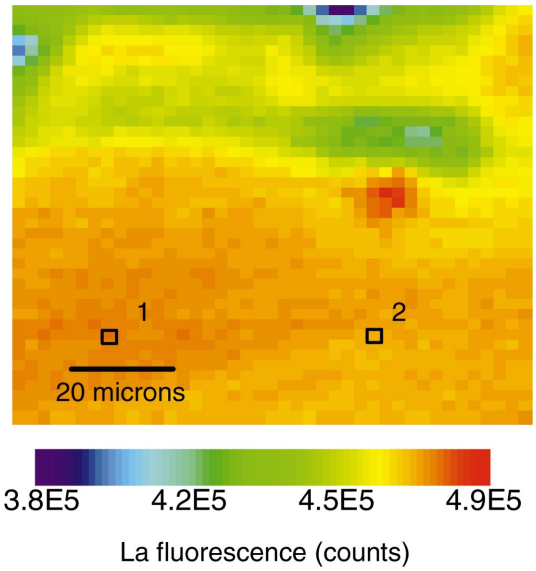

FIG. 2. (Color) A 100×100 μm^2 image of the bilayer $LaSrMn_2O_7$ obtained by scanning the sample through the microfocused beam while recording the La $L_{\alpha,\beta,\gamma}$ fluorescence at each 2.5×2.5 μm^2 pixel. Red (blue) corresponds to high (low) fluorescence counts and thus to high (low) La concentration. The bar at the bottom illustrates colors associated with intermediate concentrations. The error bars are equal to the square root of the number of counts. The pixels labeled 1 and 2 are positions on the sample that vary in La concentration by approximately 1%. XMCD vs temperature curves at each of these points are presented in Fig. 3.

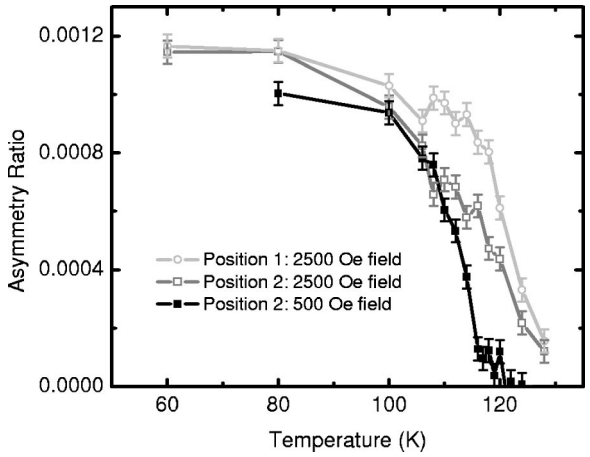

FIG. 3. Asymmetry ratio measured in a bilayer $LaSrMn_2O_7$ sample at the two positions on the sample labeled in Fig. 2. The measurements were performed with the incident x rays tuned near the Mn K edge. The gray and light gray curves were measured under an applied magnetic field of 2500 Oe, and the black curve was measured under an applied magnetic field of 600 Oe.

no greater than 70 kHz for XMCD measurements where the detector dead time is insignificant. The dead-time corrections to the output count rate are not accurate to the 0.1% level required to resolve the XMCD signals. At higher count rates, these corrections are necessary since the optics used to reverse the incident beam helicity also produce a small ~5% change in the incident beam intensity. We should note that this change in intensity upon helicity reversal does not affect the ion chamber since it was operated in the linear regime. Furthermore, because the phase-retarding optics use the transmitted part of the beam, the beam position is constant regardless of x-ray helicity. Therefore, neither the ion chamber nor the phase-retarding optics limited the resolution of the experiment.

III. APPLICATIONS OF THE TECHNIQUE

We present results from two experiments to demonstrate the effectiveness and capability of the low-temperature scanning element-specific magnetic microscopy instrument. The first example illustrates the ability to measure local magnetization as a function of temperature in a single-crystal doped manganese oxide bilayer $La_{1.2}Sr_{1.8}Mn_2O_7$ sample. The preparation of this sample is described in Ref. 14. Figure 2 shows a 100×100 μm^2 image (2.5 μm steps) of the La concentration taken using the low-temperature magnetic microscopy setup. The chemical contrast was measured by tuning the energy of the incident beam above the La L_3 edge ($E=5.489$ keV) and monitoring the La fluorescence. To enhance the sensitivity to differences in La concentration, we subtracted a background image taken below ($E=5.460$ keV) the La L_3 edge. Red regions in Fig. 2 correspond to regions of high La concentration, and blue corresponds to low La concentration. The scans performed to obtain the image in Fig. 2 required a total of 12 h of data acquisition. Large variations in the La concentrations occurred near the top of the image as indicated by the green and blue regions. The total variation across the scanned region is on the order of 20% here, which is greater than the variation expected to cause the percolation nature of the phase transition; therefore, we concentrated our measurements on the regions labeled 1 and 2 on the sample. Here, the variation is only 1.2%, which is more consistent with the models of previous experimental results.[15] With the count rates achieved here, the technique is sensitive to chemical concentration variation of 0.1%.

We performed localized measurements of the magnetization versus temperature at the two regions labeled in Fig. 2 by measuring the magnitude of the XMCD signal versus temperature in the fluorescence channel. XMCD measures the difference in absorption of a sample with the helicity of an incoming circularly polarized beam parallel and antiparallel to the local magnetization direction of the absorbing atom. This difference is proportional to the component of the net magnetization along the photon wave vector and as such provides an element-specific analog to superconducting quantum interference device (SQUID) measurements. In the fluorescence channel, the difference in fluorescence intensity measured with opposite helicities of the incident x rays, I^+-I^-, normalized by the sum, $(I^+-I^-)/(I^++I^-)$, is defined as the asymmetry ratio (AR), such that $AR\propto|M|\cos\theta$, where M is the net magnetization, and θ is the angle between the magnetization and the photon wave vector.

In $La_{1.2}Sr_{1.8}Mn_2O_7$, Mn carries the magnetic moment; the measurements were performed at $E=6.552$ keV, which corresponds to the maximum in the XMCD signal near the Mn K edge. The results are presented in Fig. 3, in which the gray circles and light-gray squares correspond to the XMCD magnitude versus temperature measured at positions 1 and 2 in Fig. 2, respectively. Due to the small size of the XMCD

signal (~0.1%), measurements were taken for opposite orientations of the applied magnetic field, and the average plotted. Switching the field direction is equivalent to reversing the helicity of the incoming beam and allows us to eliminate any experimental artifacts arising from detector dead-time issues mentioned in Sec. II or long-term drifts in the incident beam intensity. Including field and helicity reversals, each data point in Fig. 3 took approximately 30 min to acquire. Magnetization curves were obtained with two different values of the applied magnetic field, 0.6 and 2.5 kOe. Measurements taken at the higher applied magnetic field (2.5 kOe) reveal a pronounced difference in the magnetic transition temperature at the two positions. Furthermore the region of higher La concentration (position 1) exhibits a steeper decrease of the magnetization, whereas the magnetization with the lower La concentration region exhibits a more gradual decrease. The measurements at low field (0.6 kOe), shown by the black symbols in Fig. 3, gave similar results for both regions. The higher transition temperature for the greater applied magnetic field strength is consistent with previous results obtained on these materials.[16] The results are also consistent with other studies that indicate different paramagnetic-to-ferromagnetic transition temperature with La concentration.[17] By repeating scans over the same regions of the sample, we did not notice any changes of sample position under the reversal of the applied magnetic field.

In the next set of results presented, we applied the low-temperature element-specific magnetic microscopy instrument to the multiferroic composite mixture system: (x)LSMO$(1-x)$LMO, where x indicates the molar ratio of the two compounds. Figure 4 presents microfocused images of composite mixtures of the form (x)LSMO$(1-x)$LMO with $x=0.21$ and $x=0.23$ obtained by scanning the sample through the 4×4 μm^2 microfocused beam while recording the fluorescence counts with 2×2 μm^2 steps (oversampling by a factor of 2). In Figs. 4(a) and 4(c), the La $L_{\alpha,\beta,\gamma}$ fluorescence lines were recorded, and in Fig. 4(b), the Lu L_{α} fluorescence line was recorded. Red (blue) corresponds to high (low) fluorescence counts and thus to high (low) La concentration in (a), (c) or high (low) Lu concentration in (b). The images in (a)–(c) are 200×200 μm^2 and were obtained at room temperature. Each of the images required 5 h of data acquisition. Images of the chemical contrast obtained at 25 K look qualitatively similar to those taken at room temperature. The x-ray images illustrate how the LSMO and LMO are immiscible as shown by the islands of LMO in the LSMO in Figs. 4(a) and 4(b). The immiscibility of the LMO and LSMO appears to occur on different length scales. The regions of LSMO as shown in red in Fig. 4(a) are ~10 μm, and the regions of LMO as shown in blue are ~25–50 μm in length. The green regions in this image show that the immiscibility of these two phases can also be smaller than our resolution in some regions. In Fig. 4(c), the LSMO forms islands of ~10 μm in length within the LMO. With a very small change in the concentration of LSMO, from $x=0.21$ to 0.23, the sample morphology changed significantly. The change in morphology may have some dependence on x but is most likely associated with different sample preparation techniques.[18] We focused the magnetic measurements on the $x=0.23$ sample.

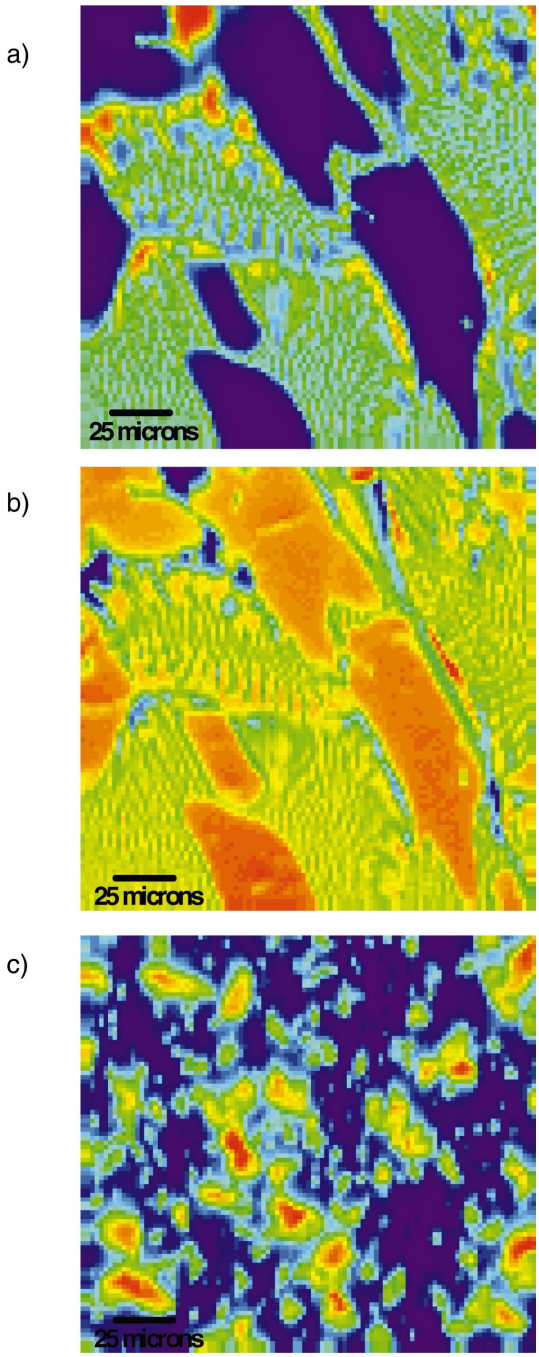

FIG. 4. (Color) Microimaging of the $x=0.21$ (a)–(b) and $x=0.23$ (c) (x)LSMO:$(1-x)$LMO composite samples obtained by scanning the sample through the microfocused beam while recording the fluorescence counts at each 2×2 μm^2 pixel. In (a), (c), the La $L_{\alpha,\beta,\gamma}$ fluorescence lines were recorded, and in (b), the Lu L_{α} fluorescence line was recorded. Red (blue) corresponds to high (low) fluorescence counts and thus to high (low) La concentration in (a), (c) or high (low) Lu concentration in (b). The coloring convention is the same as in Fig. 2. The images are all 200×200 μm^2 and were obtained at room temperature. The error bars are equal to the square root of the number of counts.

To correlate the magnetic structure with the observed LSMO grains shown in Fig. 4(c), the strength of the XMCD signal under an applied field of 5 kOe at 25 K was measured in the fluorescence channel. The magnitude of the field was sufficient to saturate the magnetization in the LSMO.[3] Consequently, the asymmetry ratio was recorded at 6.539 keV, which coincided with the largest XMCD signal, while scan-

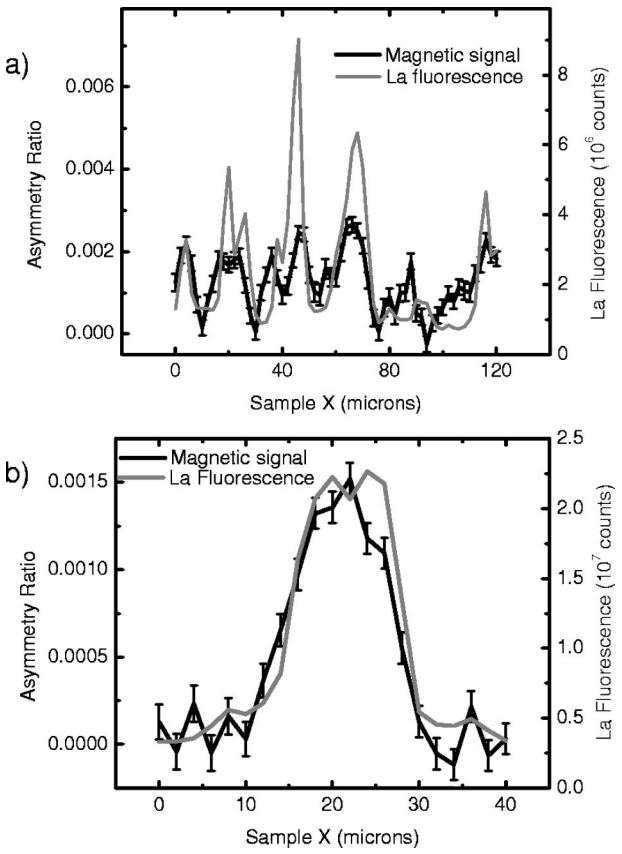

FIG. 5. La fluorescence and the asymmetry ratio measured near the Mn *K* edge vs horizontal sample position in μm for the $x=0.23$ LSMO:LMO composite sample at $T=25$ K. The plot in (a) is over a 120 μm length that has approximately five grains of LSMO, corresponding to peaks in the La fluorescence. The plot in (b) is over a single grain of LSMO. The error bars associated with the La fluorescence are equal to the square root of the number of counts and are smaller than the lines representing the La fluorescence signal.

ning the sample position through the beam. The results of two of these scans are presented in Fig. 5. In the first scan, we translated the sample by 120 μm through the incident beam, while recording La fluorescence and Mn fluorescence simultaneously. As the helicity of the x rays was switched, the Mn *K*-edge fluorescence was measured as I^+ and I^-, and then the asymmetry ratio was recorded. From Fig. 5, we see a nearly exact correlation between where the LSMO regions are (peaks in the gray curve) to the positive values of the asymmetry ratio (peaks in the black curve). Still, the signal quality is too low to obtain quantitative correlations between LSMO and the magnitude of the magnetic signal. To acquire the data in Fig. 5(a) required 7 h of beam time, so to be able to observe any difference in the magnetic domains from the chemical domains, we realistically needed to perform scans over smaller regions of the sample. Figure 5(b) presents one such scan over a 40 μm long portion of the sample that took 2.5 h of data acquisition time. Here again, we see a correlation between the La concentration (gray) and the magnetic signal (black). To within our resolution of ~ 2 μm, the magnetic domains directly overlap with the chemical domains. It is possible that chemical inhomogeneities at the nanoscale will play an important role in the magnetic phases of the systems studied here. Ultimately using this technique, one would want to look at domain structure at the nanoscale level. The experimental setup described in this article is one step toward that resolution.

IV. DISCUSSION

In this article, we have described a technique for low-temperature element-specific magnetic microscopy under a moderate applied magnetic field. The temperature and applied magnetic field ranges accessible with this setup allowed us to study two systems of doped manganese oxides. We were able to resolve chemical inhomogeneitites in a manganite sample to within fractions of 1%. The experiments on the bilayer $La_{1.2}Sr_{1.8}Mn_2O_7$ system at low temperatures have demonstrated how the inhomogeneities are related to different paramagnetic-to-ferromagnetic transition behaviors. Experiments on a composite system of ferromagnetic metallic material and antiferromagnetic insulating material have shown how this setup can be used to image magnetic domains and correlate them with chemical domains in bulk samples. Currently, the system is limited in resolution by the focusing of the x-ray beam by the bending KB mirrors; the stability of such mirrors limits the focusing to the μm scale. In the future, one may improve on the system by using KB mirrors that have a fixed bend for focusing or other focusing optics like Fresnel zone plates that have been used previously in magnetic microscopy experiments.[19,20] Full-field microscopy at low temperature under moderate applied fields may also become viable to address some of the same problems. One of the main limitations of the technique is the ability to count all of the fluorescence photons. The detectors need to be improved significantly if one is to measure magnetic domains at the transition-metal *K* edges over large regions of sample as a function of field and temperature.

ACKNOWLEDGMENTS

The authors thank M. Jaski, J. Humbert, D. Capatina, and S. Sasaki for design and construction of the electromagnet used in the experiment. They also thank M. McDowell for significant help in the setup of the experimental apparatus. Research at the Advanced Photon Source is supported by the U. S. Department of Energy, Office of Science, under Contract No. W-31-109-ENG-38.

[1] L. Vasiliu-Doloc *et al.*, Phys. Rev. Lett. **83**, 4393 (1999).
[2] A. Moreo, S. Yunoki, and E. Dagotto, Science **283**, 2034 (1999).
[3] S. Park, N. Hur, S. Guha, and S.-W. Cheong, Phys. Rev. Lett. **92**, 167206 (2004).
[4] S. Anders *et al.*, Rev. Sci. Instrum. **70**, 3973 (1999).
[5] C. M. Schneider and G. Schönhense, Rep. Prog. Phys. **65**, R1785 (2002).
[6] X-S. Zhu *et al.* , Rev. Sci. Instrum. **74**, 4718 (2003).
[7] D. Peterka, A. Enders, G. Haas, and K. Kern, Rev. Sci. Instrum. **74**, 2744 (2003).
[8] J. W. Freeland, J. C. Lang, G. Srajer, R. Winarski, D. Shu, and D. M. Mills, Rev. Sci. Instrum. **73**, 1408 (2002).
[9] R. J. Dejus, B. Lai, L. R. Moog, and E. Gluskin, Argonne National Laboratory Rep. No. ANL/APS/TB-17 (1993).
[10] J. C. Lang and George Srajer, Rev. Sci. Instrum. **66**, 1540 (1995).
[11] B. X. Yang, M. Rivers, W. Schildkamp, and P. J. Eng, Rev. Sci. Instrum. **66**, 2278 (1995).
[12] P. J. Eng, M. Newville, M. L. Rivers, and S. R. Sutton, Proc. SPIE **3449**, 145 (1998).
[13] L. Feng, J. S. Iwancyk, B. E. Patt, S. Barkan, and C. R. Tull, Proc. SPIE

5198, 103 (2004).
[14] J. F. Mitchell, D. N. Argyriou, J. D. Jorgensen, D. G. Hinks, C. D. Potter, and S. D. Bader, Phys. Rev. B **55**, 63 (1997).
[15] S. Rosenkranz, R. Osborn, L. Vasiliu-Doloc, J. W. Lynn, S. K. Sinha, and J. F. Mitchell, cond-mat/9909059.
[16] A. Berger, J. F. Mitchell, D. J. Miller, and S. D. Bader, J. Appl. Phys. **89**, 6851 (2001).
[17] M. Medarde, J. F. Mitchell, J. E. Millburn, S. Short, and J. D. Jorgensen, Phys. Rev. Lett. **83**, 1223 (1999)
[18] The $x=0.21$ sample [imaged in Figs. 4(a) and 4(b)] was melted using the optical floating zone method, then solidified. The melting temperature is greater than 1500 °C. The $x=0.23$ sample [imaged in Fig. 4(c)] is a polycrystalline specimen prepared through conventional solid-state reaction in air. The sample was sintered at 1400 °C for 48 h with intermediate grindings, followed by annealing in an oxygen environment. No melting or liquid phase was involved in the preparation of the polycrystalline sample.
[19] J. Pollmann, G. Srajer, J. Maser, J. C. Lang, C. S. Nelson, and C. T. Venkataraman, Rev. Sci. Instrum. **71**, 2386 (2000).
[20] J. C. Lang, J. Pollmann, D. Haskel, G. Srajer, J. Maser, J. S. Jiang, and S. D. Bader, Proc. SPIE **4499**, 1 (2001).